Advanced Steel Construction – Vol. 22 No. 2 (2026) 153–169
DOI:10.18057/IJASC.2026.22.2.3

EXPERIMENTAL STUDY ON FLEXURAL PERFORMANCE OF LARGE-SECTION PARTIALLY ENCASED COMPOSITE BEAM WITH WEB OPENINGS

Hong-Xin Liu [1, 2], Ping Yang [3], Yu-Kun Yang [4], Jie Li [5], Ya-Ming Li [1, 2], Shui-Zhong Jia [1, 2] and Xiao-Meng Xie [4, *]

[1] *Shanghai Institute of Architectural Design and Research Co., Ltd., Shanghai 200041, China*
[2] *Shanghai Engineering Research Center of Spatial Structure, Shanghai 200041, China*
[3] *The Government Investment Project Proxy Construction Center of Kangbashi District, Ordos City, Erdos 017000, China*
[4] *Shanghai Jieyi Construction Technology Co., Ltd., Shanghai 201311, China*
[5] *Tongji University, Shanghai 201206, China*
** (Corresponding author: E-mail: xiexiaomeng2024@163.com)*

ABSTRACT

To investigate the effect of openings on the flexural performance of large-section partially encased composite beams (referred to as large-section PEC beams), static tests were conducted on five large-section PEC beams with different configurations. The study focused on the influence of web openings in the primary and secondary beams on the flexural performance, ductility, and failure modes of the specimens under four-point bending. The results indicate that under static loading, all specimens exhibited good ductility, with strength-to-yield ratios ranging from 1.18 to 1.30, and retained some strength reserves after reaching the yield load. Web openings slightly reduced the load-bearing capacity and sectional stiffness of the specimens. The strain in the main steel component and the concrete strain along the section height approximately exhibited a linear distribution, conforming to the plane section assumption. A finite element model was developed based on the test results. The load-deflection curves and stress contours matched well with the experimental results, and the error between the simulated and experimental ultimate load-bearing capacities was within 10%. The flexural load-bearing capacity calculated using the proposed method for large-section PEC beams with web openings showed minor deviations from the experimental values, with minimal influence from size effects, confirming the safety and reliability of the adopted formulas.

ARTICLE HISTORY

Received: 16 March 2025
Revised: 29 June 2025
Accepted: 2 July 2025

KEYWORDS

Large-section PEC beams;
Failure mode;
Flexural capacity;
Ductility;
Finite element analysis

Copyright © 2026 by The Hong Kong Institute of Steel Construction. All rights reserved.

1. Introduction

Steel-concrete composite beams represent a hybrid structural form that integrates the high compressive capacity of concrete with the tensile strength and ductility of steel materials [1–4]. These composite systems have seen broad adoption in bridge engineering, industrial buildings, and various civil structures due to their excellent stiffness, strong load-bearing ability, and limited deformation under service loads [5–8]. A specific form of such systems, known as partially encased composite (PEC) members, is produced by embedding shear connectors into the flanges of steel profiles and casting concrete around them [9]. During the prefabrication process, PEC components require only lateral formwork, thereby simplifying the construction procedure. The concrete confined within the flange regions significantly mitigates the likelihood of both overall and local buckling, thus contributing to a higher structural capacity [10–11]. When compared to traditional steel components, PEC beams display marked improvements in fire resistance [12–13], as well as notable enhancements in flexural and shear behavior [14–15], which has led to growing interest in their application both in domestic and international contexts.

To date, extensive research has been carried out on the mechanical behavior and practical applications of PEC beams. Nakamura et al. [16] demonstrated that, compared with conventional I-section steel beams, the flexural and shear load-bearing capacities of PEC beams are increased by factors of 2.08 and 2.98, respectively. Through both experimental studies and numerical modeling, He et al. [17–18] identified that PEC beams with corrugated steel webs possess enhanced shear resistance and greater fracture modulus, and further introduced a corresponding shear capacity calculation approach. Nardin et al. [19] focused on how construction methods influence the flexural behavior of PEC beams, concluding from experimental observations that bottom bolts contribute to an increase in fracture modulus. In a study by Kindmann et al. [20], 12 PEC beams featuring different cross-sectional configurations were subjected to bending tests, which confirmed that concrete encased within flanges contributes positively to both flexural stiffness and capacity. Furthermore, the adoption of advanced concrete materials with improved tensile performance has led to notable enhancements in the flexural behavior of steel-concrete composite beams [21–23]. Hao et al. [24] performed shear tests on PEC-UHPC composite beams, revealing their exceptional performance in resisting shear forces.

Compared to traditional steel beams, PEC beams exhibit improved load-bearing capacity and ductility. However, the concrete poured into the web increases the component's weight and cost, and the segmented casting process required for PEC beams reduces construction efficiency. To address these issues, it is common practice to introduce web openings in the steel web. These openings serve multiple engineering purposes: they reduce structural self-weight, facilitate the passage of mechanical, electrical, and plumbing (MEP) systems through the beam, and eliminate the need for flipping the beam for casting—thus enabling one-sided formwork and continuous concrete pouring, which significantly improves constructability and efficiency. Compared to traditional PEC beams, PEC beams with web openings enhance material utilization and simplify construction. Recent studies have begun to explore this configuration. Zhao et al. [25], for instance, proposed two new types of honeycomb PEC beams and investigated the effects of web openings, compressed steel flanges, and filled concrete on the mechanical performance of beams.

However, their study was limited to small-span specimens with relatively modest cross-sectional dimensions. In practical applications, large-section PEC beams are often needed to satisfy increasing span and load requirements that exceed the capacity of conventional PEC configurations. These large-section beams also benefit from web perforations, which help reduce self-weight and support single-pass, one-sided casting without flipping, thereby improving production efficiency. In this study, experimental and finite element investigations were conducted on large-section PEC beams with various forms and sizes of process openings in the web. The failure modes, load-bearing capacity, main steel strain, component deformation, and ductility were analyzed to examine the influence of web openings on the flexural performance of large-section PEC beams. A calculation method for the flexural load-bearing capacity of large-section PEC beams was also proposed.

2. Experimental program

2.1. Specimen design

The specimens were developed in accordance with the *Technical Specification for Partially Encased Steel-Concrete Composite Structures* (T/CECS 719—2020) [26], and were labeled as PECB1 (primary beam), PECB2 (secondary beam), PECB3 (primary beam with web openings type 1), PECB4 (secondary beam with web openings), and PECB5 (primary beam with web openings type 2). All tested beams feature cross-sectional heights greater than 600 mm, thus qualifying as large-section PEC beams. The main steel members were fabricated using Q355-B steel, while HRB400 steel was utilized for both tie rods and anti-crack reinforcement. C30-grade concrete was applied in the web regions. The designed span length l_0 was 10,800 mm for PECB1, PECB3, and PECB5, and 7,200 mm for PECB2 and PECB4. Fig. 1 provides the detailed structural layout of each specimen.

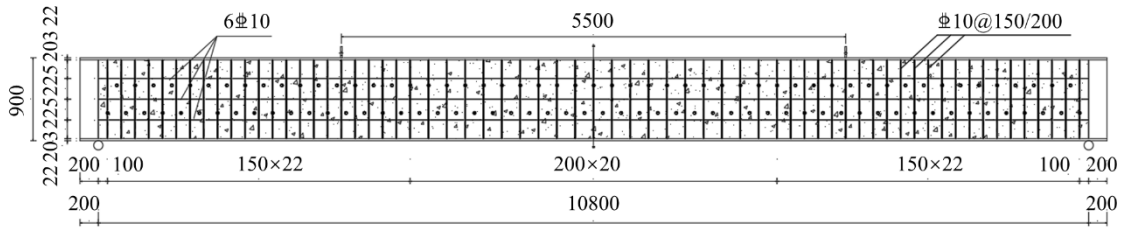

(a) Specimen PECB1 elevation

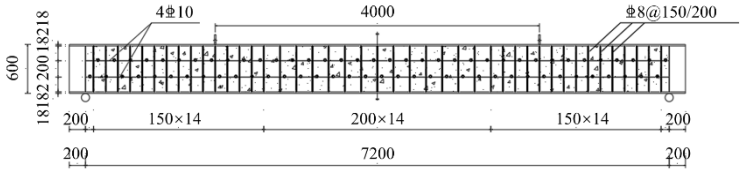

(b) Specimen PECB2 elevation

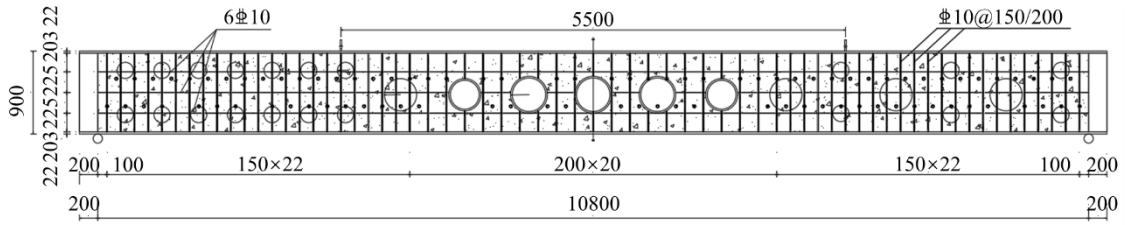

(c) Specimen PECB3 elevation

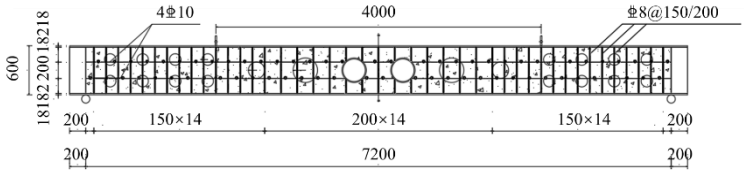

(d) Specimen PECB4 elevation

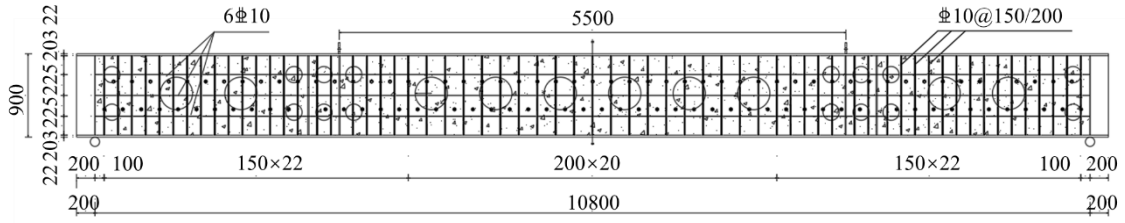

(e) Specimen PECB5 elevation

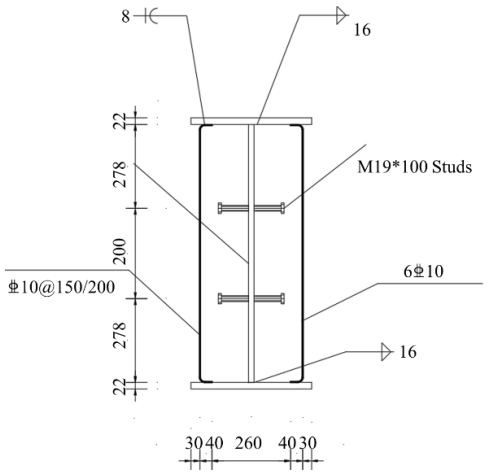

(f) Middle section of main beam span

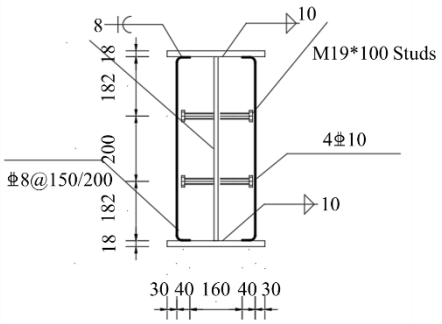

(g) Mid-span section of secondary beam

Fig. 1 Schematic diagram of PEC beams

Table 1
Basic parameters of specimen design

Number	Calculated length l_0 /mm	Height h_a / mm	Width b_f / mm	Flange thickness t_f / mm	Web thickness t_w / mm	Steel ratio / %	Web opening ratio / %
PECB1	10800	900	400	22	18	8.63	-
PECB2	7200	600	300	18	12	9.04	-
PECB3	10800	900	400	22	18	8.63	15.36
PECB4	7200	600	300	18	12	9.04	17.98
PECB5	10800	900	400	22	18	8.63	14.56

The key geometric and material parameters are summarized in Table 1. In specimen PECB3, web openings included five unfilled holes at midspan with a diameter of 400 mm, quarter-span holes of 350 mm, and additional openings of 175 mm. For PECB4, midspan openings measured 300 mm in diameter (with two left unfilled), quarter-span openings were 200 mm, and the remaining were 140 mm. In contrast, PECB5 adopted a midspan opening diameter of 350 mm and 175 mm for the others, with all web perforations fully filled with concrete to accommodate the casting process. The spacing of tie rods was arranged at 200 mm within the pure bending region and reduced to 150 mm in the bending-shear transition zone. The steel ratio for the section was computed exclusively based on the cross-sectional area of structural steel components.

2.2. Material properties

The material property tests for the concrete were conducted in the Building Materials Laboratory at Tongji University, following the national standard testing method "Standard for Test Methods of Physical and Mechanical Properties of Concrete" (GB/T50081-2019)[27]. Under the same curing conditions, the compressive strength of the concrete cube is 31.1 MPa. The material properties of the steel were determined according to the "Tensile test method for metal materials at room temperature " (GB/T 228.1-2010) [28]. Standard tensile tests were performed using the universal testing machine in the Structural Engineering Laboratory at Tongji University, with the loading apparatus shown in Fig. 3. All steel plates used for the specimens were taken from the same batch of steel and were cut into proportional samples for testing. The yield strength f_y, ultimate strength f_u, and elastic modulus E of the steel materials with different thicknesses are listed in Table 2.

Table 2
Material properties of steel

Number	t/mm	f_y/MPa	f_u/MPa	E/MPa
1	12	408.13	524.31	231378
2	18	390.81	488.79	223478
3	22	408.49	499.13	215244

2.3. Loading protocol and measurement

Specimens PECB1, PECB3, and PECB5, which have larger spans and higher cross-sectional load-bearing capacities, were subjected to monotonic loading using two 350-ton actuators. The loading points were located at the one-third points of the span, with the specific loading setup shown in Fig. 2(a). Specimens PECB2 and PECB4, which have smaller spans and lower cross-sectional load-bearing capacities, were tested using a single 350-ton actuator. The vertical concentrated load applied by the actuator was distributed to the test specimens through a rigid distribution beam. The loading points were located at one-third of the calculated span, with the specific loading setup shown in Fig. 2(b). To achieve simply supported boundary conditions, one end of the specimens was configured as a sliding hinge support, while the other end was a fixed hinge support.

(a) Loading device of PECB1, PECB3 and PECB5 specimens

(b) Loading device of PECB2 and PECB4 specimens

Fig. 2 Specimen loading diagram

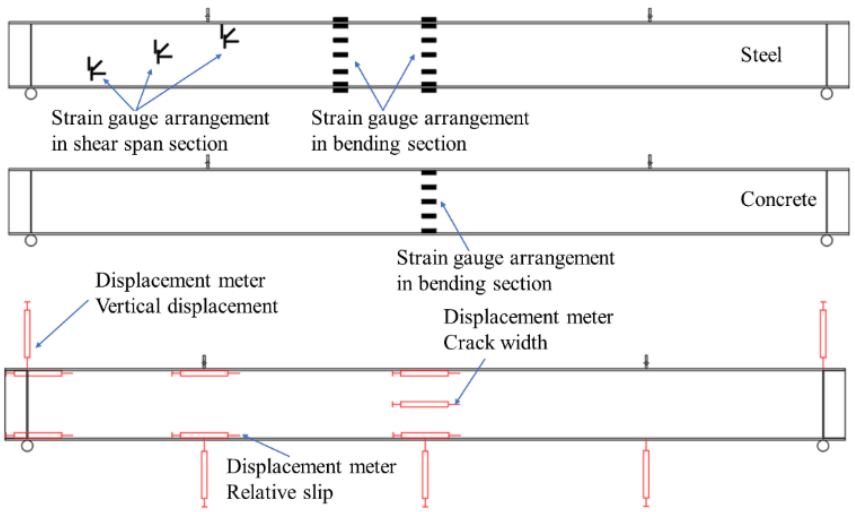

Fig. 3 Displacement gauge and strain gauge layout

The formal loading process adopted a force-controlled loading phase followed by a displacement-controlled loading phase. For specimens PECB1, PECB3, and PECB5, each of the two jacks applied 60 kN per loading step (approximately 0.05 P_u, where P_u is the ultimate load of the beam) at a loading rate of 20 kN/min. For specimens PECB2 and PECB4, the load per step was 30 kN (approximately 0.05 P_u) at a loading rate of 10 kN/min. After reaching half

of the estimated ultimate load (calculated as the yield load using the transformed section method), the control mode was switched to displacement-controlled loading, with each step increasing by 5 mm at a rate of 5 mm/min. Loading continued until the specimen failed, ensuring that the deflection at the loading point exceeded 300 mm within the effective stroke of the jack. The specific layout of the test measurement points is shown in Fig. 3.

3. Experimental results analysis

3.1. Failure pattern of specimen

Specimen PECB1 entered the cracked working stage after being loaded to 348.2 kN (approximately 0.11 P_u). The midspan deflection at this point was 5.35 mm (l_0/2019). At 1397.3 kN (approximately 0.45 P_u), the maximum midspan crack width reached the serviceability limit (0.3 mm), and the midspan deflection was 28.88 mm (l_0/374). At 2640.8 kN (approximately 0.85 P_u), the midspan deflection exceeded the serviceability limit (l_0/200), and the yield strain (2700 με) was reached in the upper and lower steel flanges. The midspan deflection was 81.62 mm (l_0/132). At 3090.2 kN (P_u), partial spalling of the top surface concrete at the midspan occurred. The midspan deflection exceeded 1/50 of the calculated span, meeting the failure criteria for the specimen, and the test was terminated. The pure bending zone at the final failure of specimen PECB1 is shown in Fig. 4.

Specimen PECB2 entered the cracked working stage after being loaded to 193.5 kN (approximately 0.11 P_u), with a midspan deflection of 4.04 mm (l_0 /1881). At 1276.6 kN (approximately 0.70 P_u), the midspan deflection exceeded the serviceability limit (l_0/200), reaching 48.57 mm (l_0/156). At 1560.9 kN (approximately 0.86 P_u), the maximum crack width on both sides of the midspan reached the serviceability limit (0.3 mm). The upper and lower steel flanges achieved the yield strain (2400 με), and the midspan deflection was 79.33 mm (l_0/96). At 1813.6 kN (P_u), slight spalling occurred on the top surface concrete at the midspan. The midspan deflection exceeded 1/50 of the calculated span, reaching the failure criteria for the specimen, and the test was terminated. The pure bending zone at the final failure of specimen PECB2 is shown in Fig. 5.

(a) Specimen failure diagram

(b) North side area

(c) Mid-span region

(d) South side area

Fig. 4 Final failure state of specimen PECB1

(a) Specimen failure diagram

(b) North side area

(c) Mid-span region

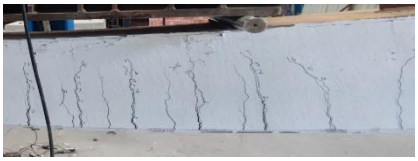

(d) South side area

Fig. 5 Final failure state of specimen PECB2

(a) Specimen failure diagram

(b) North side area

(c) Mid-span region

(d) South side area

Fig. 6 Final failure state of specimen PECB3

Specimen PECB3 entered the cracked working stage after being loaded to 339.9 kN (approximately 0.11 P_u), with a midspan deflection of 5.70 mm (l_0/1896). At 2140.4 kN (approximately 0.69 P_u), the midspan deflection approached the serviceability limit (l_0/200), and the maximum crack width on both sides reached the serviceability limit (0.3 mm). The midspan deflection was 53.37 mm (l_0/202). At 2463.8 kN (approximately 0.79 P_u), the upper and lower steel flanges achieved the yield strain (2700 με), and the midspan deflection was 86.63 mm (l_0/125). At 3107.9 kN (P_u), abnormal noises were heard, and partial spalling occurred on the top surface concrete at the midspan. The midspan deflection exceeded 1/50 of the calculated span, meeting the failure criteria, and

the test was terminated. The pure bending zone at the final failure of specimen PECB3 is shown in Fig. 6.

Specimen PECB4 entered the cracked working stage after being loaded to 413.9 kN (approximately 0.23 P_u), with a midspan deflection of 10.17 mm (l_0 /708). At 1244.5 kN (approximately 0.70 P_u), the midspan deflection exceeded the serviceability limit (l_0/200), reaching 36.82 mm (l_0/195). At 1450.6 kN (approximately 0.82 P_u), the maximum crack width on both sides of the midspan reached the serviceability limit (0.3 mm), and the midspan deflection reached 79.33 mm (l_0/96). At 1627.5 kN (0.92 P_u), the upper and lower steel flanges achieved the yield strain (2700 με), and the midspan deflection reached 117.65 mm (l_0/61). At 1776.7 kN (P_u), partial spalling occurred on the top surface concrete at the midspan, and cracks at the web openings became more pronounced. The midspan deflection exceeded 1/50 of the calculated span, meeting the failure criteria, and the test was terminated. The pure bending zone at the final failure of specimen PECB4 is shown in Fig. 7.

(a) Specimen failure diagram (b) North side area

(c) Mid-span region (d) South side area

Fig. 7 Final failure state of specimen PECB4

Specimen PECB5 entered the cracked working stage after being loaded to 646.8 kN (approximately 0.21 P_u), with a midspan deflection of 10.17 mm (l_0 /708). At 2284.7 kN (approximately 0.74 P_u), the upper and lower steel flanges achieved the yield strain (2700 με), the midspan deflection exceeded the serviceability limit (l_0/200), and the maximum crack width on both sides of the midspan reached the serviceability limit (0.3 mm). The midspan deflection was 71.17 mm (l_0/152). At 3100.1 kN (P_u), partial spalling occurred on the top surface concrete at the midspan. The midspan deflection exceeded 1/50 of the calculated span, meeting the failure criteria, and the test was terminated. The pure bending zone at the final failure of specimen PECB5 is shown in Fig. 8.

Compared with the unfilled specimen PECB3, PECB5 exhibited significantly different cracking behavior in the region surrounding the web openings. Due to the presence of concrete infill, no radiating or diagonal cracks were observed extending from the hole edges. Instead, the cracks remained primarily vertical and concentrated in the pure bending zone, with more uniform distribution and smaller crack widths. This indicates that the concrete filling within the web openings helped to redistribute internal stresses and reduce stress concentrations at the hole periphery, thereby effectively suppressing the development of radial cracks. The improved crack pattern also contributed to more stable crack propagation and delayed local damage near the openings, as evidenced by the relatively intact concrete surface shown in Fig. 8.

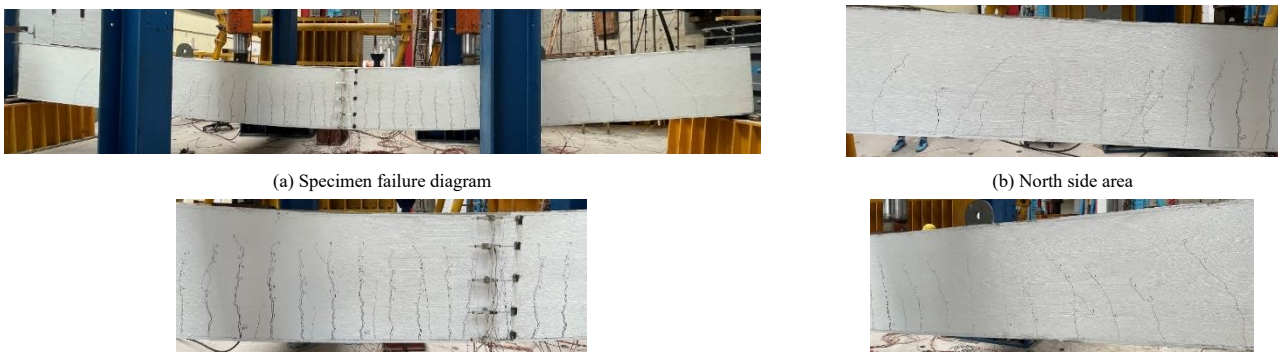

(a) Specimen failure diagram (b) North side area

(c) Mid-span region (d) South side area

Fig. 8 Final failure state of specimen PECB5

In summary, all five specimens initially exhibited concrete cracking, followed by steel flange yielding and eventual spalling of the top concrete surface at midspan, with midspan deflections exceeding the failure criteria. Notably, in specimens with unfilled web openings such as PECB3, the altered load transfer path around the openings led to the formation of radiating cracks extending downward from the hole edges. These cracks were accompanied by wider crack widths and more pronounced spalling and bulging of the concrete above the openings. In contrast, specimens with filled openings, such as PECB5, exhibited predominantly vertical cracks without significant radiating patterns, and the surrounding concrete remained largely intact. These observations indicate that concrete infill effectively mitigates local stress concentrations and inhibits the development of radial cracking.

3.2. Load-mid-span deflection curve

Fig. 9 presents the load–midspan deflection curves for the test specimens, which can be clearly divided into two behavioral phases. (1) Elastic Stage: Prior to the yielding of the tensile flange, the concrete is effectively restrained by the main steel structure and the reinforcement, resulting in slow crack initiation and negligible stiffness degradation. During this phase, the load–deflection relationship remains largely linear. (2) Elasto-plastic Stage: Once the tensile flange yields, the specimen enters a stage characterized by inelastic behavior. Cracks in the web concrete begin to propagate rapidly, diminishing their structural contribution and causing a gradual reduction in sectional stiffness. The corresponding deflection curve develops noticeable inflection points and deviates from linearity, showing increased midspan displacement and clear bending deformation. With continued loading, the bottom flange of the main steel component undergoes strain hardening, which helps maintain the flexural capacity of the section. Subsequently, as the upper flange yields, partial spalling of the concrete at the midspan top surface is observed. At this stage, the deflection approaches the allowable limit, marking the termination point of the test.

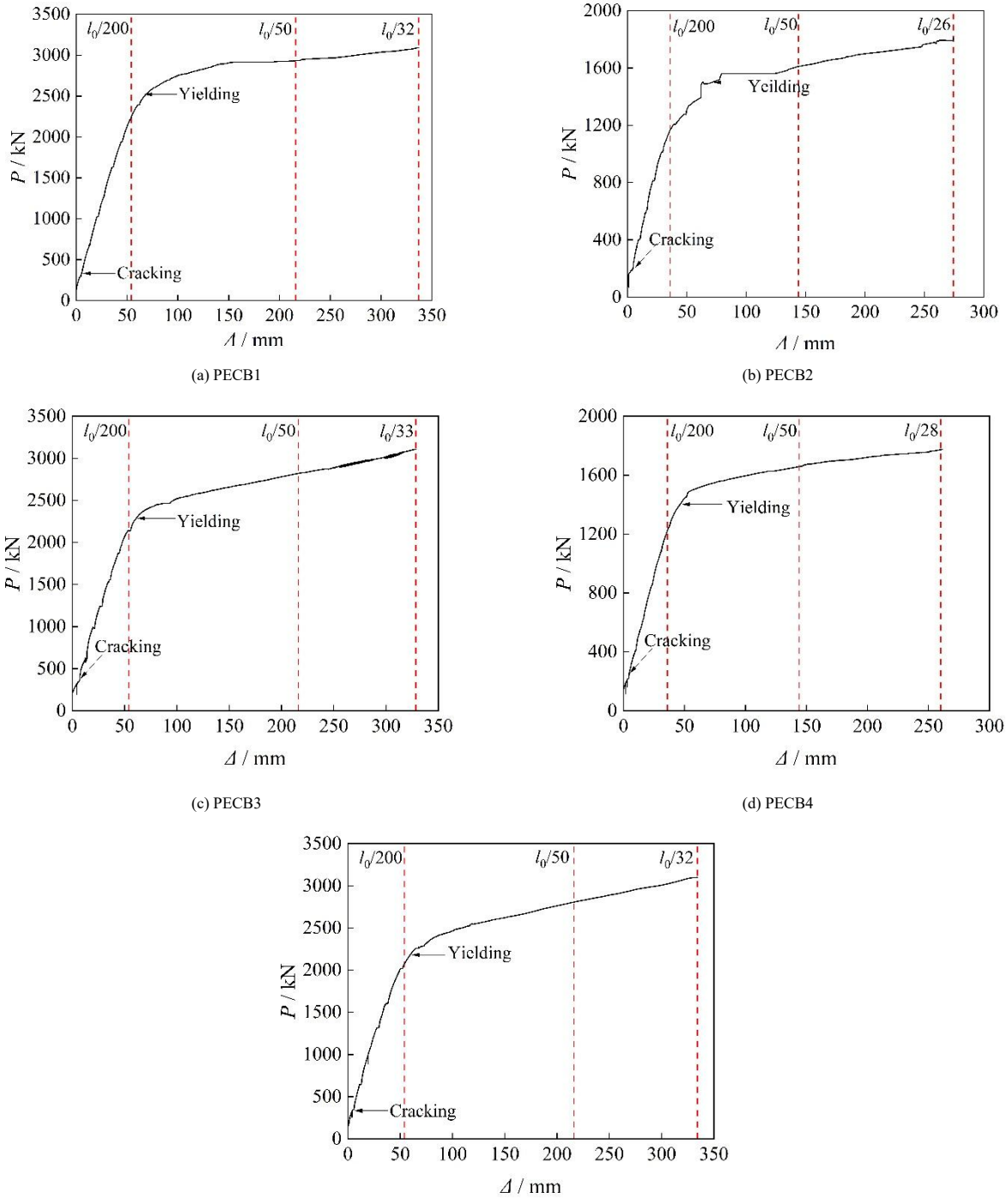

Fig. 9 Load-mid-span deflection curve

By comparing the load-midspan deflection curves of specimens with and without web openings, it was observed that the initial stiffness showed minimal differences. This limited variation arises because, although the presence of web openings reduces the cross-sectional rigidity of the primary steel structure, the effect is largely offset by the presence of concrete infill and added reinforcement. Once the specimens enter the yielding phase, PECB1 exhibits marginally higher load-carrying capacity than PECB3 and PECB5. Nevertheless, at the ultimate failure point, their capacities converge to nearly identical values. Meanwhile, PECB2 and PECB4 display similar curve patterns without notable divergence. These findings suggest that while web openings cause a slight decrease in load-bearing capacity, their overall influence remains minor. This is attributed to the fact that the flexural resistance of PEC beams is predominantly governed by the steel flanges, web, and concrete, with the web itself contributing a comparatively smaller share.

3.3. Bearing capacity analysis

Based on the load-midspan deflection curves of the specimens, the load-bearing capacities and displacements at characteristic points are summarized in Table 3. The theoretical cracking load P_{cr}' was calculated using the "Technical Specification for Partially Encased Composite Steel-Concrete Structures" (T/CECS 719—2020)[26], while the actual cracking load P_{cr} was obtained experimentally. The theoretical yield load P_y' was calculated using the yield stress obtained from material tests based on the edge yield criterion, and the actual yield load P_y was measured experimentally using the Park method. The theoretical ultimate load P_u' was derived using the full-section plasticity criterion, and the actual ultimate load P_u was determined experimentally. The ductility coefficient μ was used to evaluate the ductility performance of the specimens, defined as $\mu=\Delta_u/\Delta_y$, where Δ_u is the ultimate displacement, and Δ_y is the yield displacement.

As shown in Table 3: (1) The experimental load values at characteristic points of the specimens were higher than the calculated values, indicating that the load-bearing capacity can be determined using the edge yield criterion and the full-section plasticity criterion. (2) The cracking load of the specimens ranged from 0.1 P_u to 0.2 P_u, indicating early cracking. This was likely due to the presence of initial cracks in the concrete. However, the crack development

met the requirements of the specifications, and the load-bearing capacity exceeded 0.7 P_u at the normal serviceability limit state. (3) The overstrength ratio of the specimens ranged from 1.18 to 1.30, indicating that the specimens retained a certain strength reserve after reaching the yield load. (4) All specimens exhibited stable post-yield behavior and excellent ductility, with ductility coefficients exceeding 4.0, indicating strong deformation capacity and energy dissipation potential suitable for seismic design applications. (5) Compared to specimen PECB1, the yield strength of specimens PECB3 and PECB5 decreased by 6.0% and 8.4%, respectively, while their yield displacements increased by 5.2% and 6.0%, respectively. The yield strength and yield displacement of specimens PECB2 and PECB4 showed minimal differences, indicating that large-section PEC beams are more significantly affected by web openings in the steel section.

Table 3
Bearing capacity and displacement of characteristic points

Number	Web opening ratio / %	Stiffness /N·mm^{-1}	Cracking load / kN		Yielding load / kN		Δ_y/mm	P_y / P_y'	Ultimate load /kN		Δ_u / mm	P_u / P_u'	P_u / P_y	μ
			P_{cr}'	P_{cr}	P_y'	P_y			P_u'	P_u				
PECB1	-	33516	155.4	348.2	2185.4	2605.9	77.75	1.19	2734.5	3090.2	336.88	1.07	1.19	4.33
PECB2	-	23804	88.7	193.5	1241.6	1504.2	63.19	1.21	1474.4	1813.6	274.38	1.32	1.21	4.34
PECB3	15.36	29947	155.4	339.9	2185.4	2450.3	81.82	1.12	2734.5	3107.9	328.44	1.31	1.27	4.01
PECB4	17.98	24997	88.7	201.5	1241.6	1511.1	60.45	1.22	1474.4	1776.7	261.27	1.14	1.18	4.32
PECB5	14.56	28953	155.4	323.4	2185.4	2386.6	82.43	1.09	2734.5	3100.1	334.16	1.13	1.30	4.05

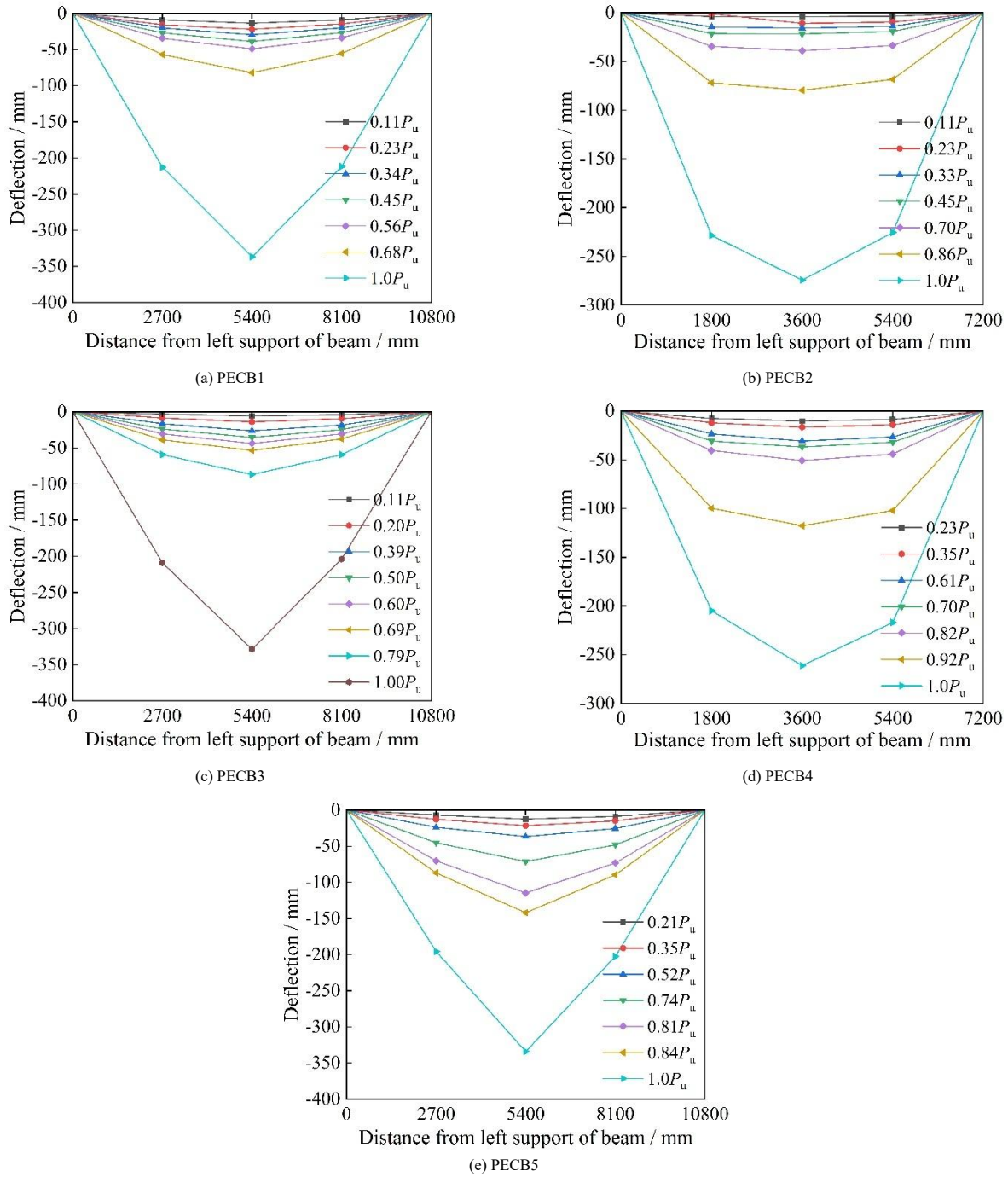

(a) PECB1

(b) PECB2

(c) PECB3

(d) PECB4

(e) PECB5

Fig. 10 Specimen deformation

3.4. Deformation analysis

Beams with good ductility can absorb a certain amount of energy after reaching their yield or maximum load-bearing state, exhibiting strong post-yield deformation capacity and providing clear warnings or deformations before failure. Fig. 10 illustrates the vertical deformations at various locations on the specimens, and the following observations can be made: (1) All specimens exhibited excellent ductility, with ductility coefficients exceeding 4.0, indicating strong ductile performance. (2) When the load reached approximately 0.7P_u, the deflection reached the serviceability limit state deflection value (l_0/200). (3) At the initial loading stage, specimen deformations were minimal, with similar deflections observed at the 1/4-span and 3/4-span points. Before the yield load, the deformations of the specimens gradually increased at a slow rate. After reaching the yield load, the rate of deflection growth significantly increased, indicating that the specimens had entered the elasto-plastic stage.

3.5. Cross-section strain distribution

To evaluate the distribution pattern of deformation along the cross-sectional height of the main steel member and concrete in the pure bending zone of large-section PEC beams under load, two control cross-sections were established in the pure bending zone of the specimens. Strain gauges (BX120-100AA) were evenly spaced and arranged on the concrete and web, while displacement meters with a range of 10 mm were evenly spaced and installed on the surface of the concrete on the opposite side. Both strain gauges and displacement meters were placed on the concrete surface to account for potential damage to the strain gauges due to tensile cracking when the deformation of the concrete became significant, as displacement meters can still roughly measure the progression of concrete strain. The strain development of the steel flanges under load is illustrated in Fig. 11. At the initial loading stage, the strain in the flanges generally exhibited a linear increase with the load. When the load reached approximately 0.7P_u to 0.8 P_u, the strain in both the upper and lower flanges reached the yield strain. Upon further loading, the flange strain increased rapidly, and the strain curve began to show an inflection point, consistent with the load-deflection curve at mid-span.

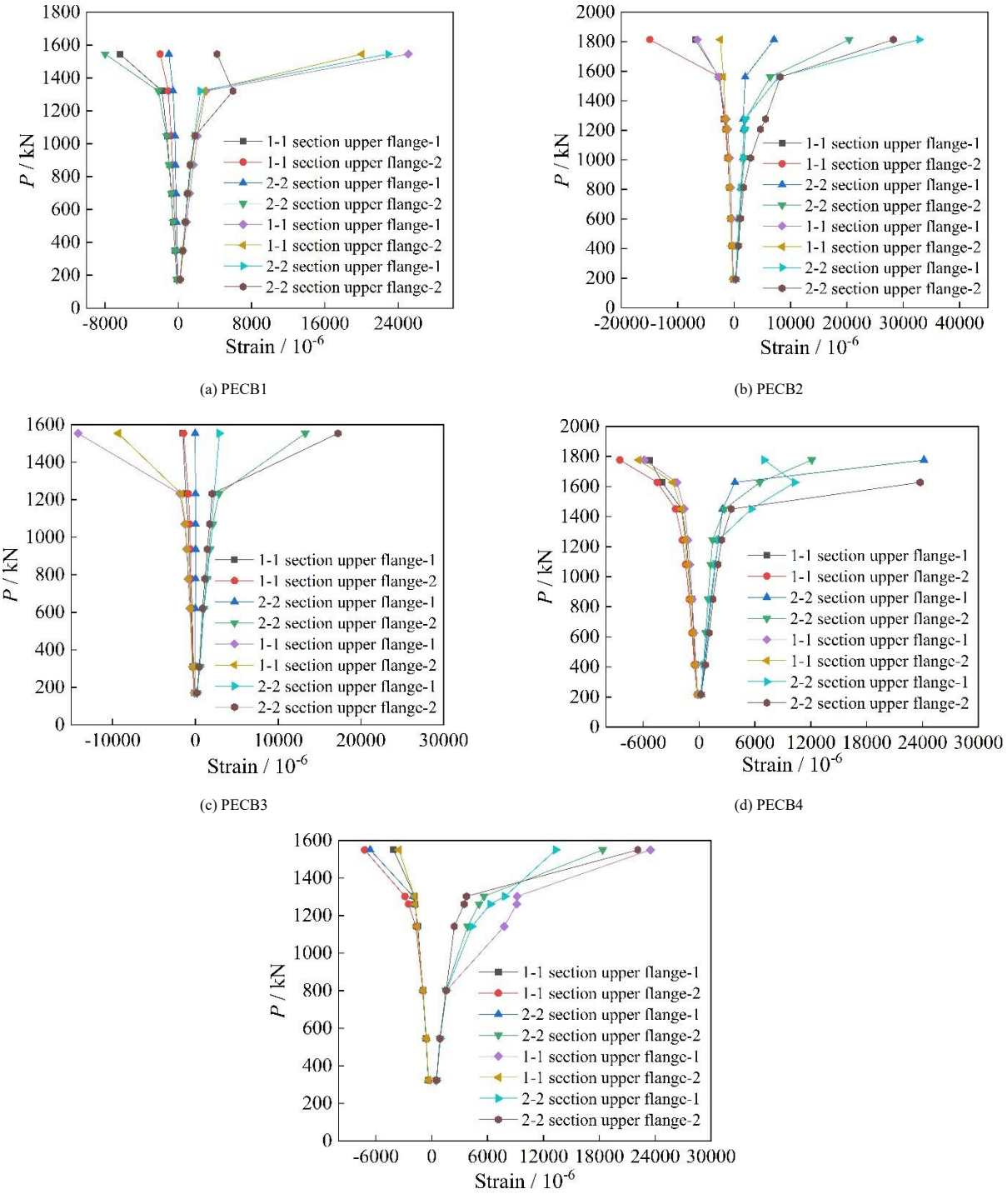

(a) PECB1

(b) PECB2

(c) PECB3

(d) PECB4

(e) PECB5

Fig. 11 Flange strain of the specimen

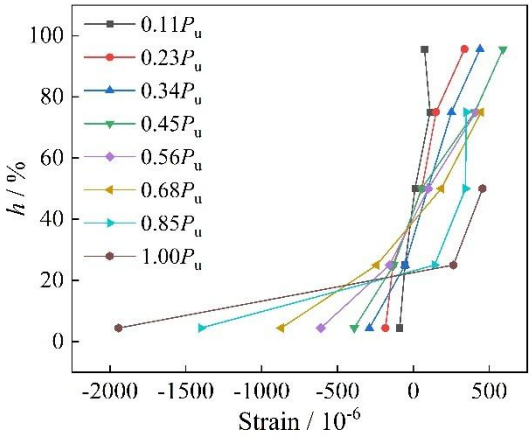

(a) PECB1

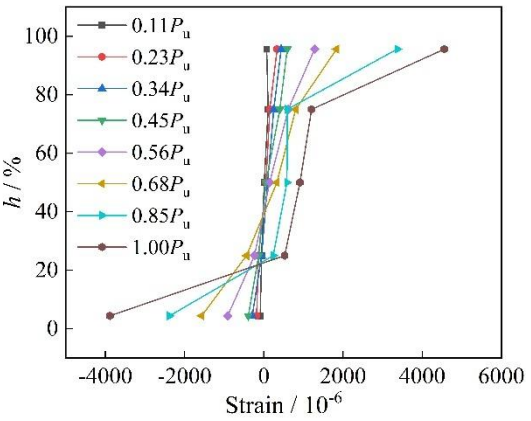

(a) PECB1

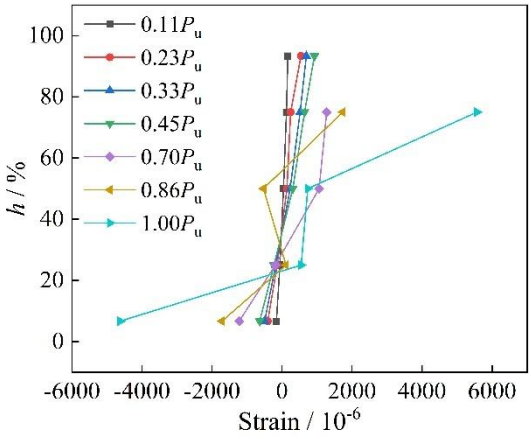

(b) PECB2

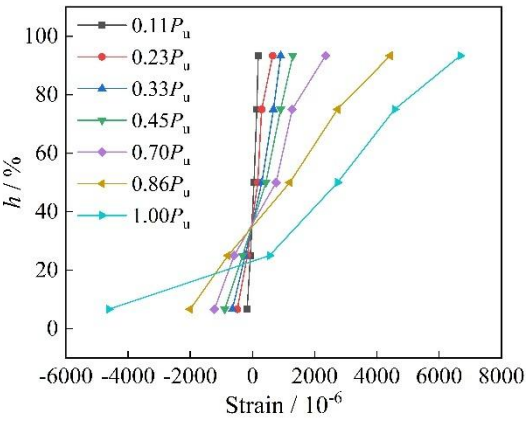

(b) PECB2

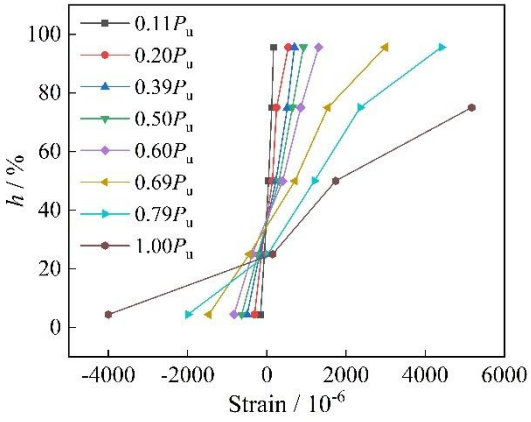

(c) PECB3

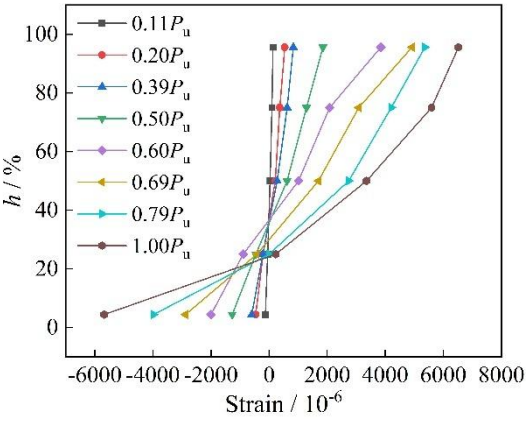

(c) PECB3

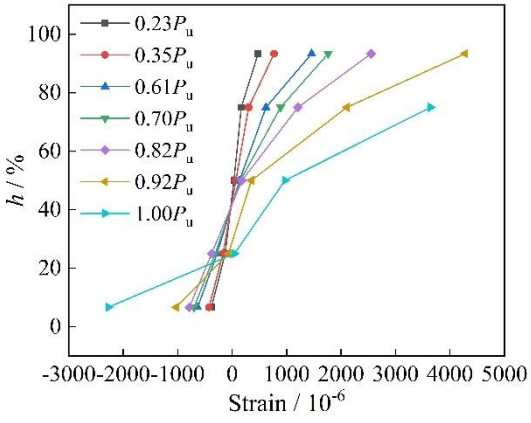

(d) PECB4

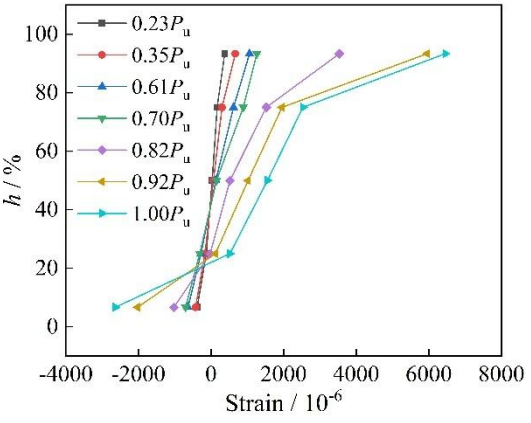

(d) PECB4

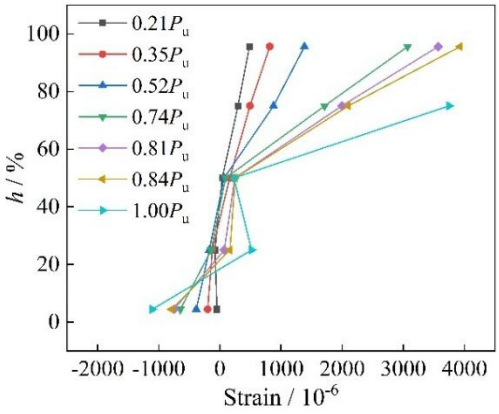

(e) PECB5

Fig. 12 Strain of section steel web

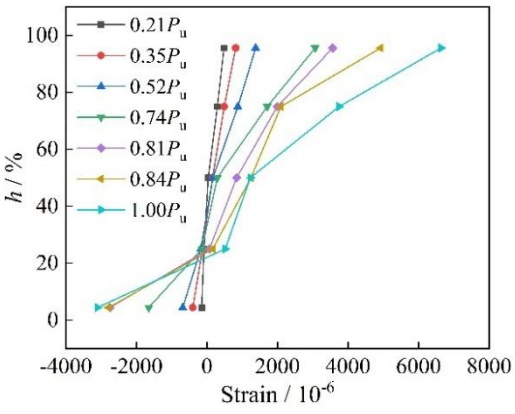

(e) PECB5

Fig. 13 Concrete strain

Fig. 12 and Fig. 13 illustrates the strain curves of mid-span concrete and steel along the cross-sectional height, where h represents the height from the lower flange. Before reaching a load of $0.7P_u$, the neutral axis of the cross-sections for specimens PECB1, PECB3, and PECB5 was approximately located at a height of 450 mm. For specimens PECB2 and PECB4, the neutral axis was approximately located at a height of 250 mm, and the strains in concrete and steel along the cross-sectional height conformed to the plane section assumption. After the load reached $0.7P_u$, the tensile strain in the concrete increased, the neutral axis of the cross-section shifted significantly upward, and severe cracking occurred in the web concrete, leading to stress redistribution and a somewhat nonlinear strain distribution across the cross-section.

4. Finite element analysis of large-section PEC beams

4.1. Finite element modelling

This numerical model is developed to replicate the failure behavior of PEC beams subjected to quasi-static loading. It integrates multiple geometric elements and force interactions. The steel reinforcement and link components are represented using the two-node three-dimensional truss element (T3D2), while the concrete and steel beam components are modeled with eight-node solid hexahedral elements featuring reduced integration (C3D8R). A structured meshing strategy is employed, applying a consistent element size of 100 mm across all components, including steel, concrete, links, longitudinal reinforcement, and construction steel. Details of the mesh partitioning are illustrated in Fig. 14.

As shown in Fig. 14, the finite element model adopted a uniform mesh size of 100 mm, which was selected based on both the geometric features of the specimens and practical considerations of simulation accuracy and computational efficiency. Given that the web opening diameters ranged from 175 mm to 400 mm, and the steel web thickness was between 12 mm and 22 mm, the chosen mesh size ensures that even the smallest openings are discretized by at least 6–8 elements along the diameter. This resolution is generally sufficient to capture the stress concentration and deformation gradients near discontinuities such as holes and thin webs. Additionally, finer mesh sizes were evaluated during preliminary simulations, but no significant improvement in global load–displacement response was observed, while computational cost and convergence difficulties increased. The selected 100 mm mesh size provided stable performance and successfully reproduced key structural responses observed in the experiments.

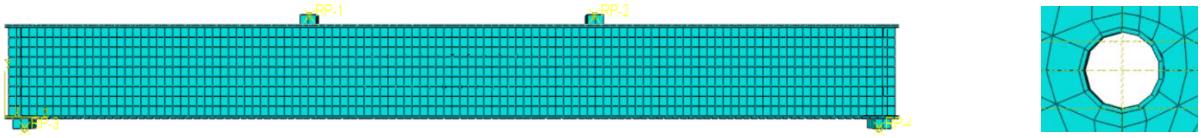

(a) Overall mesh division

(b) Mesh division at the opening

Fig. 14 Finite element model and mesh division

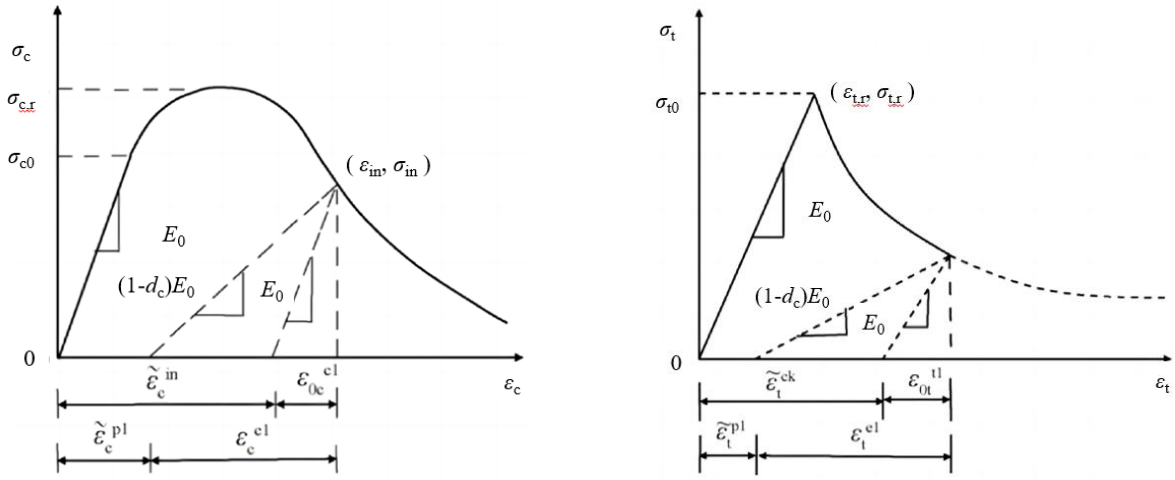

(a) Single-axis compression

(b) Single-axis tension

Fig. 15 Stress-strain relationship of concrete in CDP model

The concrete plastic damage model (CDP) is adopted to simulate concrete behavior. According to the study conducted by Chang Xinquan from Southeast University [29], excluding the damage factor can notably shorten the computation time, though it may introduce deviations in the descending segment of the concrete stress–strain response when compared to experimental observations. The constitutive models for concrete in both compression and tension, along with the corresponding damage factors, are defined based on the provisions of the "Code for Design of Concrete Structures" (GB 50010—2010) [30], and are illustrated in Fig. 15. For the CDP model, key parameters include a dilation angle of 35°, a flow potential eccentricity of 0.15, a viscosity parameter of 0.0015, a biaxial-to-uniaxial compressive yield strength ratio of 1.16, and a stress invariant ratio (K_c) of 0.6667 along the tension-compression meridian. In addition, the mechanical response of reinforcement bars and steel sections is represented using a bilinear stress–strain model in the simulation process.

In the finite element model, a paired contact interaction is defined between the concrete and steel components. Tangential behavior follows Coulomb friction theory with a friction coefficient set to 0.5, while normal interaction is modeled using hard contact. The flanges are permitted to separate outwardly from the concrete but are restricted from penetrating inward. Additionally, the ends of the link elements are rigidly connected to the flanges of the steel beam, whereas the longitudinal reinforcement bars are anchored into the end plates, all of which are embedded within the concrete. These end plates are modeled as rigid bodies, ensuring no deformation, and are bound to both the steel beam ends and concrete ends through section binding.

4.2. Comparison of numerical simulation and experimental results

4.2.1. Contrastive analysis of load-deflection curves

Fig. 16 presents the load-deflection comparison curves between the numerical simulation results and the experimental results for the bending test specimens of large-section PEC beams. It can be observed that the finite element simulation performs well, as the experimental curves align closely with the simulation curves, indicating that the selected computational model accurately captures the entire bending process of the large-section PEC beams.

To strengthen the numerical validation, Table 4 has been added to provide a comprehensive quantitative comparison between FEM simulation results and experimental data for all five specimens. The comparisons include yielding load (P_y), yielding displacement (Δ_y), ultimate load (P_u), and ultimate displacement (Δ_u), along with their respective percentage errors.

The results demonstrate that the FEM model achieves high accuracy in predicting both load and displacement at key response stages. Specifically, the error in yielding load remains within ±5% for most specimens, with the exception of PECB5 (7.82%). The error in yielding displacement is also generally low, ranging from 0.49% to 8.84%. Ultimate load predictions are particularly accurate for PECB2, PECB3, and PECB5, with errors below 1.2%, while PECB1 and PECB4 show larger deviations (11.71% and –16.97%, respectively), likely due to variations in local failure modes and damage propagation not fully captured in the model.

Moreover, the predicted ultimate displacements (Δ_u) show excellent agreement with the experimental values for all specimens, with maximum deviation below ±0.35%. This further confirms the model's capability to simulate deformation behavior under large deflections.

As noted in Fig. 16, the simulation and experiment exhibit good agreement in the overall shape of the load–displacement curve, particularly during the loading stage. However, discrepancies become apparent during the unloading phase. These deviations are mainly attributed to simplifications in the constitutive models of concrete and steel, which do not fully capture post-peak stiffness degradation, microcrack-induced softening, and interface debonding effects. Additional refinement, such as incorporating damage-plasticity models or cohesive zone elements, may improve the unloading phase simulation accuracy in future work.

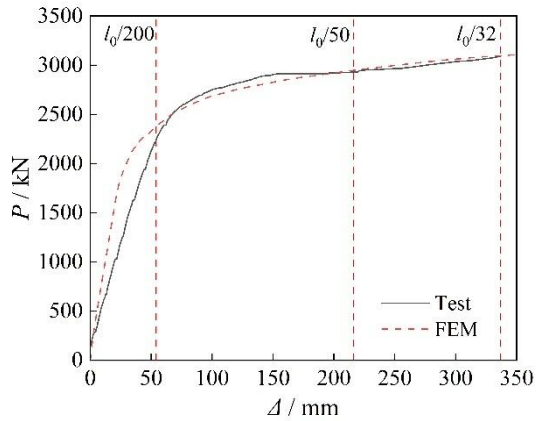

(a) PECB1

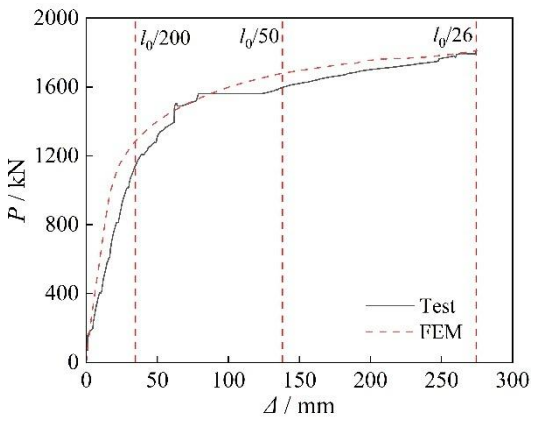

(b) PECB2

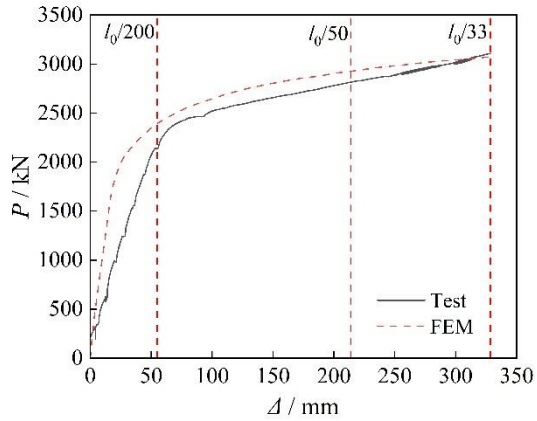

(c) PECB3

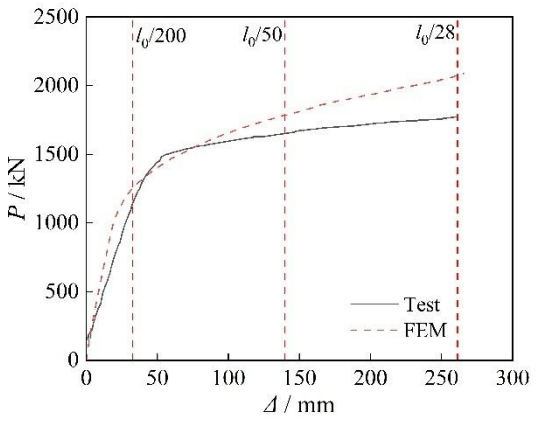

(d) PECB4

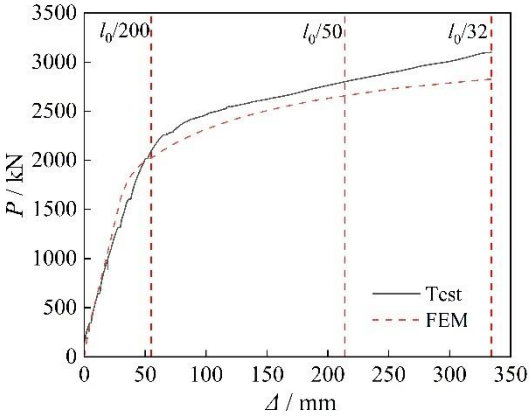

(e) PECB5

Fig. 16 Load-deflection curve comparison diagram

Table 4
Comparison between FEM simulation and experimental results

Number	Yielding load / kN		Mirror / %	Yielding displacement / mm		Mirror / %	Ultimate load /kN		Mirror / %	Ultimate displacement / mm		Mirror / %
	P_y^{FEM}	P_y		Δ_y^{FEM}	Δ_y		P_u^{FEM}	P_u		Δ_u^{FEM}	Δ_u	
PECB1	2521.5	2605.9	3.24	69.87	77.75	10.14	2734.5	3097.1	11.71	336.43	336.88	0.13
PECB2	1443.5	1504.2	4.04	57.88	63.19	8.40	1810.9	1813.6	0.15	275.01	274.38	-0.23
PECB3	2546.2	2450.3	-3.91	77.85	81.82	4.85	3073.3	3107.9	1.11	328.90	328.44	-0.14
PECB4	1446.2	1511.1	4.29	56.19	60.45	7.05	2078.2	1776.7	-16.97	262.19	261.27	-0.35
PECB5	2199.9	2386.6	7.82	78.83	82.43	4.37	2826.5	3100.1	8.83	334.48	334.16	-0.10

4.2.2. Stress distribution

Fig. 17 and Fig. 18 present the stress contour diagrams of the large-section PEC beam bending specimens under their ultimate load-bearing condition. In these figures, the maximum concrete stress is observed within the compression zone at the mid-span, with stress levels gradually diminishing toward the support ends. Similarly, the stress distribution in the steel sections shows a decreasing trend from the center of the beam outwards toward both sides.

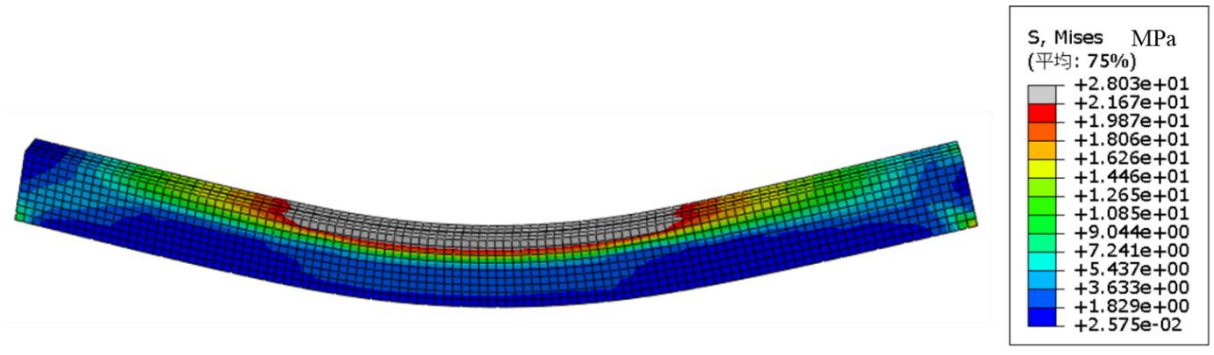

(a) PECB1

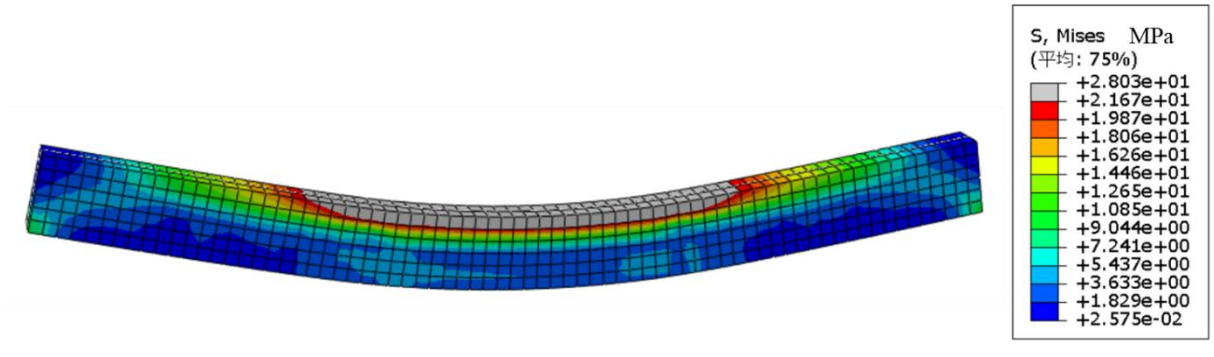

(b) PECB2

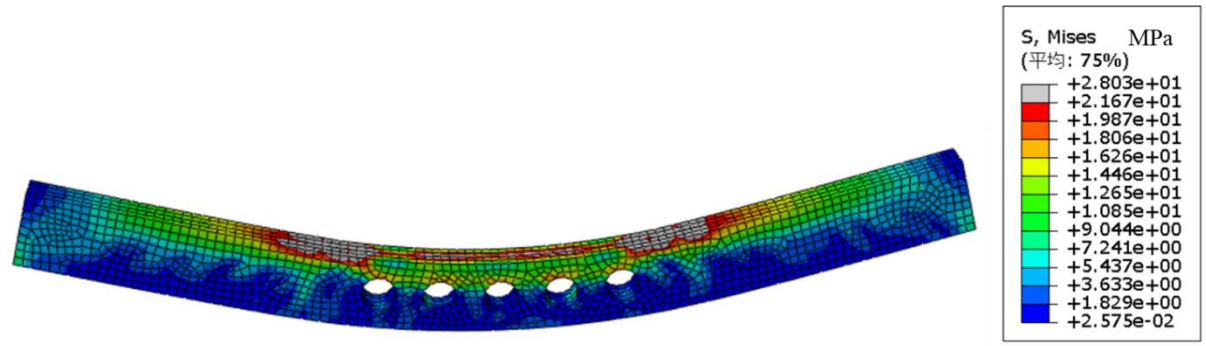

(c) PECB3

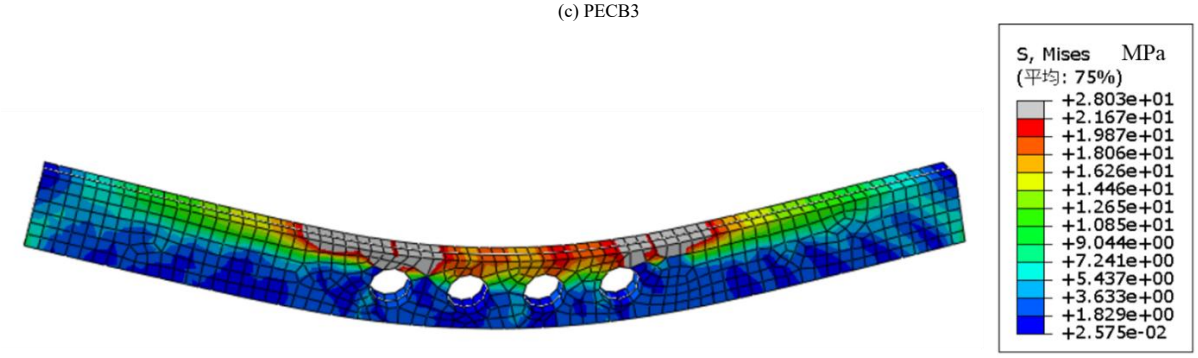

(d) PECB4

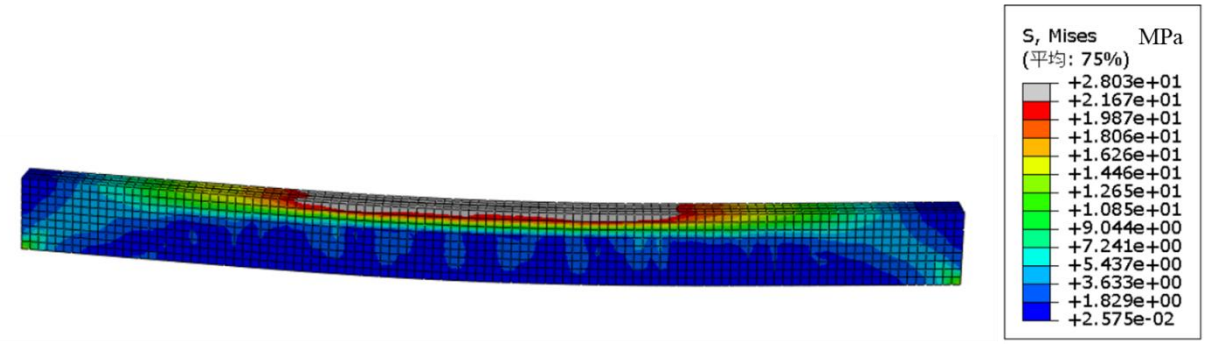

(e) PECB5

Fig. 17 Stress heat map of concrete

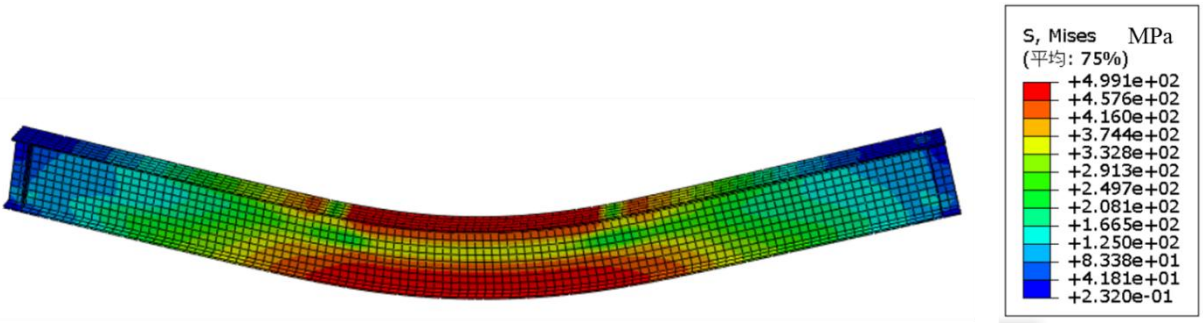

(a) PECB1

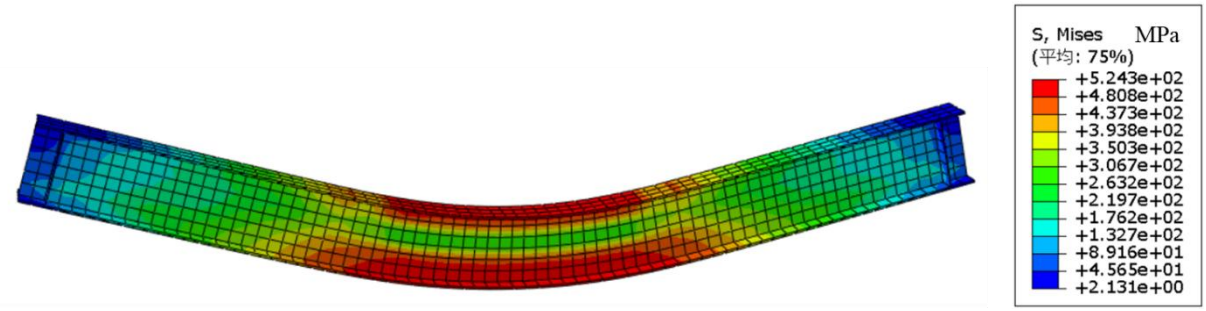

(b) PECB2

(c) PECB3

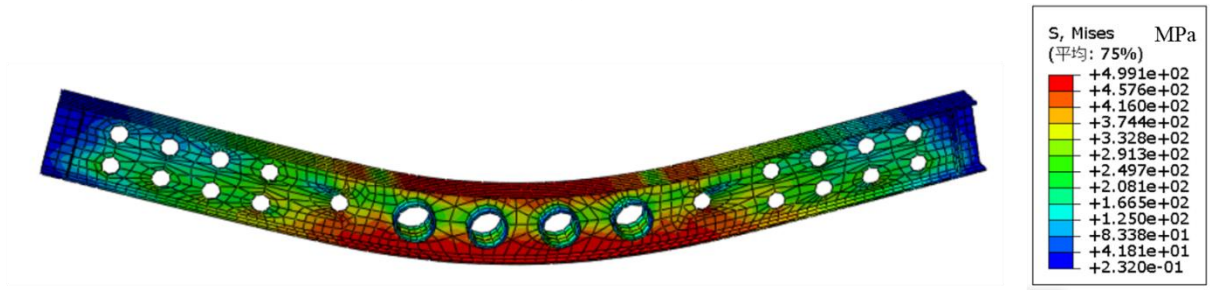

(d) PECB4

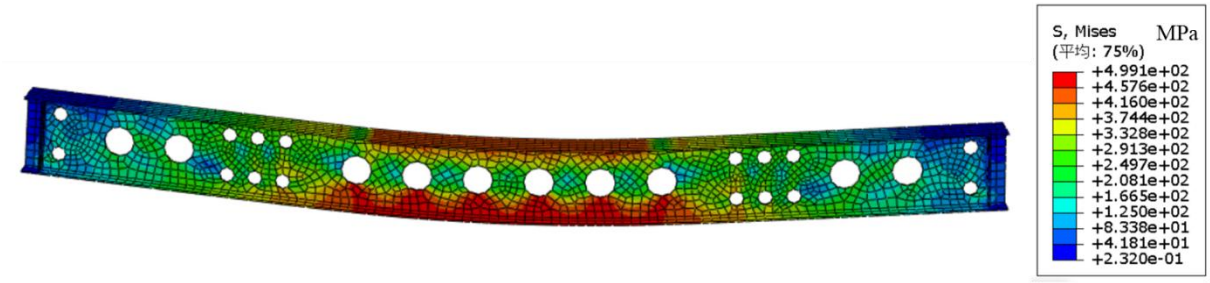

(e) PECB5

Fig. 18 Stress heat map of steel

4.2.3. Strain distribution

The plastic damage model for concrete does not simulate crack formation directly at the integration points. Instead, it visualizes crack propagation through contour representations. The direction of crack growth is determined based on the equivalent plastic strain, with the crack plane vector oriented parallel to the direction in which the maximum plastic strain occurs. The progression of cracks is presented using the distribution of maximum plastic strain values.

As shown in Fig. 19, three representative crack patterns are provided to illustrate the damage evolution process in the web concrete of large-section PEC beams. Taking specimen PECB1 as a case in point, when the applied load reaches 345 kN, tensile damage initiates at the bottom mid-span region, indicating the onset of cracking in the specimen. With the load increasing to 1400 kN, the area of tensile yielding expands, and the damage zone continues to grow. At 2100 kN, no additional tensile cracks are observed, suggesting crack saturation on the tensile side. The simulated crack development closely mirrors the observed experimental behavior, thereby confirming the accuracy and reliability of the established finite element model.

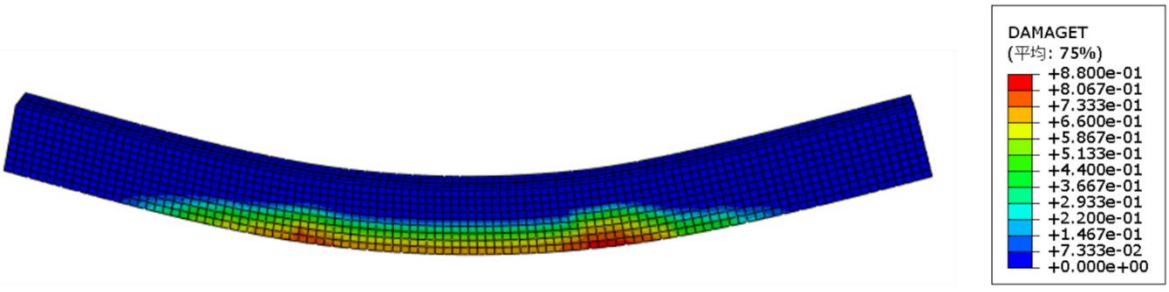

(a) P = 345 kN

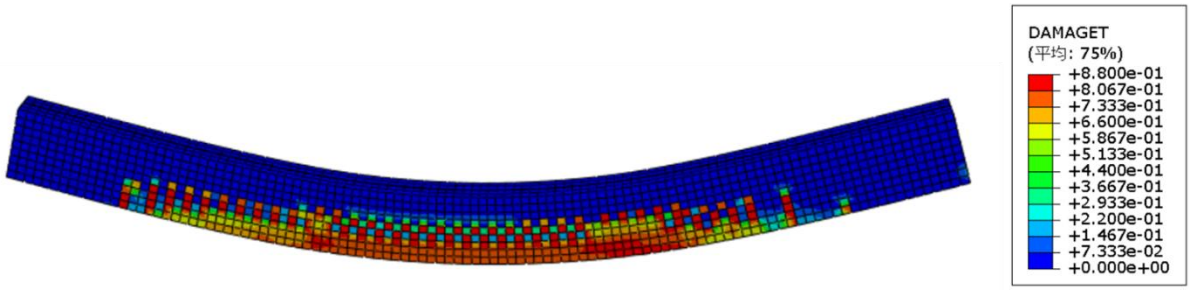

(b) P = 1400 kN

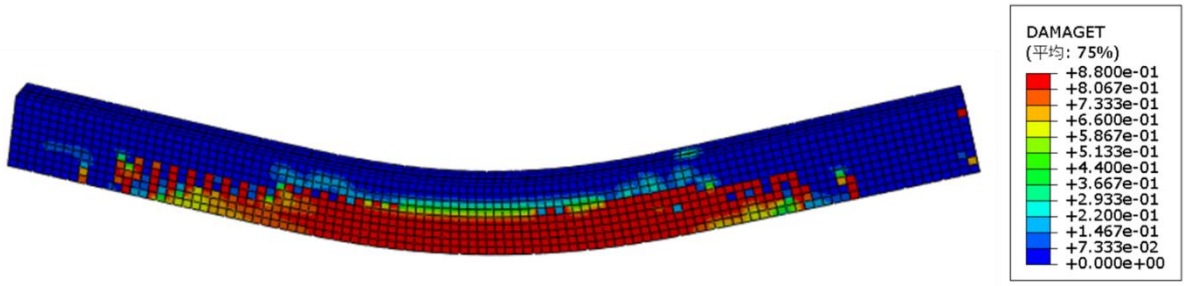

(c) P = 2100 kN

Fig. 19 Tensile strain diagram of concrete of PECB1

5. Flexural bearing capacity calculation of large-section PEC beams

The stress distribution and some parameters of the large-section PEC beam cross-section are shown in Fig. 20. During the process of reaching the ultimate load capacity, the neutral axis of the specimen continuously shifts upward, and the height of the compression zone decreases. The cross-section above the neutral axis is under compression, while the section below the neutral axis is under tension, with both the flanges and the tensile reinforcement reaching their yield strength.

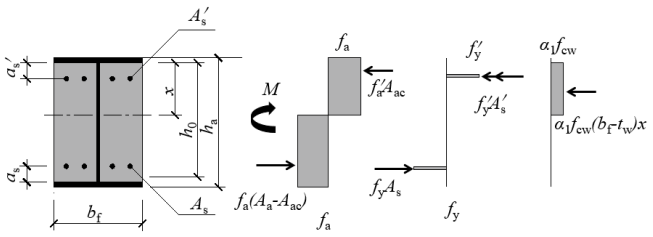

Fig. 20 Section diagram and equivalent rectangular stress diagram of large-section PEC beams

The formulas for calculating the flexural capacity of large-section PEC beams are provided in Equations (1)–(5), and the calculated results are shown in Table 5.

$$M_u = \alpha_1 f_{cw}(b_f - t_w)\frac{x^2}{2} + f_y A_s(h_a - x - 2t_f - a_s) + f_y' A_s'(x - a_s') + f_a S_{at} + f_a' S_{ac} \quad (1)$$

$$\alpha_1 f_{cw}(b_f - t_w)x + f_y' A_s' + f_a' A_{ac} - f_y A_s - f_a(A_a - A_{ac}) = 0 \quad (2)$$

$$2a_s' \le x \le \xi_b h_0 \quad (3)$$

$$\xi_b = \frac{1}{1 + \dfrac{f_y + f_a}{2 \times 0.003 E_s}} \quad (4)$$

$$A_{ac} = t_w x + b_f t_f \quad (5)$$

In these formulas: M_u represents the design value of the flexural capacity of the cross-section (N·mm); f_{cw} is the axial compressive strength design value of the concrete in the web of the main steel member (N/mm^2); x is the distance from the neutral axis of the composite section to the compression edge of the concrete (mm); h_a、b_f、t_w、t_f are the height, flange width, web thickness, and flange thickness of the main steel section of the beam (mm), respectively. α_1 is the influence coefficient of compressive stress in the compression zone; f_y、f_y' are the design values of tensile and compressive strengths of the reinforcement (N/mm^2); f_a、f_a' are the design values of tensile and compressive strengths of the main steel section of the beam (N/ mm^2); A_s、A_s' are the cross-sectional areas of the tensile and compressive reinforcement (mm^2), respectively; A_a、A_{ac} are the total cross-sectional area of the main steel section and the cross-sectional area of the compression zone of the main steel section (mm^2), respectively. a_s、a_s' are the distances from the resultant force point of the tensile reinforcement to the tensile edge of the concrete and from the resultant force point of the compressive reinforcement to the compressive edge of the concrete (mm), respectively. S_{at}、S_{ac} are the section plastic moment of the tensile and compressive areas of the main steel section relative to the plastic neutral axis of the composite section (mm^3), respectively. h_0 is the effective height of the concrete section (mm); E_a、E_s are the elastic moduli of the main steel section and the reinforcement (N/mm^2), respectively.

Table 5
The calculation results of flexural capacity are compared with the experimental results

Number	M / (kN·m)	M_u / (kN·m)	M / M_u
PECB1	5561.28	4922.12	1.13
PECB2	2296.32	1769.29	1.30
PECB3	5594.22	4922.12	1.14
PECB4	2132.04	1769.29	1.21
PECB5	5580.18	4922.13	1.13

Note: M is the test value (mid-span bending moment corresponding to ultimate load P_u).

As shown in Table 5, the experimental results for specimens PECB1, PECB3, and PECB5 were 1.13 to 1.14 times the calculated values, while those for PECB2 and PECB4 reached 1.30 and 1.21 times, respectively. These results suggest that the size effect has a measurable, though not dominant, influence on the flexural behavior of PEC beams. Specifically, the relatively higher capacity margins observed in smaller specimens (PECB2 and PECB4) may be attributed to localized constraint effects, increased relative reinforcement ratios, and reduced span-to-depth ratios, which tend to artificially enhance flexural strength. In contrast, large-section specimens (PECB1, PECB3, PECB5) exhibit more distributed cracking patterns and reduced confinement effects, leading to more realistic structural responses. This trend aligns with existing findings in the literature [31–33], which indicate that smaller-scale specimens often overestimate structural performance due to boundary and scale-induced anomalies. Overall, the good agreement between calculated and experimental values confirms the validity and safety of using the full-section plastic theory for estimating the flexural capacity of large-section PEC beams with web openings.

The average stiffness method was used in this study to calculate the average stiffness B of the specimens, and the stiffness calculations for specimens PECB3, PECB4, and PECB5 excluded the web opening regions. When calculating the equivalent sectional moment of inertia I_{ucr} for the uncracked section of large-section PEC beams and I_{cr} for the cracked section, the web concrete of the main steel member was equivalently transformed into the steel web. The calculation formulas are as follows:

$$I_{eq} = (I_{ucr} + I_{cr})/2 \quad (6)$$

In the formulas, I_{eq} represents the stiffness obtained through calculation. Using structural mechanics, the stiffness can be applied to derive the mid-span deflection f_1 of the specimen at $0.7P_u$, which is then compared with the experimentally determined mid-span deflection f at $0.7P_u$. The specific results are shown in Table 6. The deflection formula for the specimen is as follows:

$$f_1 = \frac{Pa\left(3l_0^2 - 4a^2\right)}{48B} \quad (7)$$

In the formula, f_1 is the deflection of the specimen at $0.7P_u$, l_0 is the calculated span of the specimen, a is the shear span length of the specimen, P is the load applied at the loading point, and B is the average stiffness of the specimen.

Table 6
The calculation results of mid-span deflection are compared with the test results

Number	I_{eff} / mm^4	I_{gross} / mm^4	Opening efficiency factor I_{eff}/I_{gross}	f / mm	f_1 / mm	f/f_1
PECB1	9.42×10^8	9.42×10^8	1.00	51.18	32.75	0.64
PECB2	1.80×10^8	1.80×10^8	1.00	46.65	23.94	0.51
PECB3	9.42×10^8	8.41×10^8	0.89	56.39	41.16	0.73
PECB4	1.80×10^8	1.88×10^8	1.05	36.80	29.32	0.80
PECB5	9.42×10^8	8.13×10^8	0.86	58.89	41.08	0.70

As shown in Table 6, the ratio of theoretical to experimental deflection values is consistently less than 1, indicating that in the elastoplastic stage, the calculated values tend to underestimate the actual deformation of the beams. This deviation is particularly evident in specimens with web openings (e.g., PECB3 and PECB5), where increased deflection is observed due to reduced sectional stiffness caused by perforation. To quantitatively explain this behavior, an opening efficiency factor I_{eff} / I_{gross} was introduced, where I_{eff} is estimated based on the measured average stiffness, and I_{gross} is the theoretical moment of inertia of the unperforated steel section. Given that flexural stiffness *EI* governs mid-span deflection, the calculated efficiency factors show a clear correlation with the increased deflection ratios. For example, PECB3 and PECB5, with efficiency factors of 0.894 and 0.864 respectively, correspond to increased deflection ratios f_1 / f of 0.73 and 0.70. This demonstrates that the reduction in stiffness due to web openings directly leads to larger displacements under load.

In addition, PECB2—although a solid-web specimen—exhibited the largest deflection prediction error, with f_1 / f =0.51, corresponding to a 49% underestimation. This is primarily attributed to its relatively small cross-section, which makes the specimen more sensitive to early cracking, stiffness degradation, and boundary condition effects. Moreover, the current deflection formula is based on linear elastic assumptions and does not incorporate stiffness loss from concrete cracking or localized damage. Therefore, for small-section or low-stiffness members, the simplified stiffness estimation method is less accurate. To improve predictive accuracy, future work should consider using effective moment of inertia approaches, nonlinear moment–curvature analysis, or segmental stiffness models that better reflect the post-cracking behavior of the composite section.

Therefore, the use of opening efficiency factors provides a practical design-oriented metric to assess the impact of web openings on flexural stiffness and deflection, and allows engineers to control allowable deformation levels in accordance with structural performance requirements. This refinement helps address the underestimation issue of the theoretical model and aligns well with the experimental trends observed in Table 6.

6. Conclusions

This study performed four-point bending tests on large-section PEC beams to evaluate how variables such as cross-sectional size, presence of web openings, and different opening configurations influence their failure modes, deflection response, flexural strength, ductility, and strain distribution along the section height. The principal findings are as follows:

（1）The inclusion of web openings introduces some degree of reduction in the bearing capacity of large-section PEC beams; however, the overall weakening effect is relatively minor. Compared with specimen PECB1, specimens PECB3 and PECB5 exhibited reductions in yield strength by 6.0% and 8.4%, respectively, while PECB2 and PECB4 showed no appreciable change.

（2）All tested specimens achieved ductility coefficients exceeding 4.0, indicating that large-section PEC beams possess excellent ductile behavior. The strain profiles of the primary steel elements and the surrounding concrete along the vertical section height display an approximately linear trend, consistent with the plane section assumption.

（3）The load–deflection responses and stress contour distributions from finite element simulations aligned closely with the experimental observations. The discrepancy between the simulated and measured ultimate bearing capacities was within 10%, confirming both the credibility of the adopted model and its effectiveness in capturing the flexural response of large-section PEC beams.

（4）Size effect exerts a notable influence on the flexural characteristics of PEC beams. Although large-section specimens show narrower flexural capacity margins compared to smaller counterparts, the calculated values still range from 1.13 to 1.30 times the experimental results, validating the safety and conservativeness of the proposed prediction method.

（5）The computed mid-span deflections using the reduced stiffness averaging method deviated from experimental data but did not affect the assessment of the serviceability limit state. In practice, the partial stiffness reduction caused by web openings should be considered during design to ensure structural performance.

Author Contributions

Conceptualization, Hongxin Liu; Methodology, Yukun Yang; Software, Jie Li; Resources, Yaming Li and Hongxin Liu; Writing – original draft, Shuizhong Jia; Writing – review & editing, Xiaomeng Xie; Visualization, Jie Li; Funding acquisition, Ping Yang, Yaming Li and Hongxin Liu. All authors have read and agreed to the published version of the manuscript.

Funding

Scientific Research Project of Shanghai Science and Technology Commission (21DZ1203002), Project of East China Construction Group Co., LTD. (Class 20-1-0073-Junction)

Data Availability Statement

The original contributions presented in the study are included in the article, further inquiries can be directed to the corresponding author.

Conflicts of Interest

The authors declare no conflicts of interest.

References

[1] Huang H, Xue C, Zhang W, et al. Torsion design of CFRP-CFST columns using a data-driven optimization approach[J]. Engineering Structures, 2022, 251: 113479. 10.1016/j.engstruct.2021.113479
[2] Liu J, Lyu F, Ding F X, et al. Energy dissipation of steel–concrete composite beams subjected to vertical cyclic loading[J]. Adv. Steel Constr, 2022, 18: 658-669. 10.18057/IJASC.2022.18.3.3
[3] Yan J B, Kang E C, Xie J. Behaviours of steel-concrete composite beams at low temperatures: materials and structures[J]. Adv Steel Constr, 2023, 19(4): 353-365. 10.18057/IJASC.2023.19.4.4
[4] Tian Y, Liu D, Chen X, et al. Damage evolution of steel-UHPC composite beams using AE and DIC techniques[J]. Journal of Constructional Steel Research, 2025, 224: 109163. 10.1016/j.jcsr.2024.109163
[5] Yang Y, Lin B, Zhang W. Experimental and numerical investigation of an arch–beam joint for an arch bridge[J]. Archives of Civil and Mechanical Engineering, 2023, 23(2): 101. 10.1007/s43452-023-00645-3
[6] Du Z L, Liu Y P, He J W, et al. Direct analysis method for noncompact and slender concrete-filled steel tube members[J]. Thin-Walled Structures, 2019, 135: 173-184. 10.1016/j.tws.2018.11.007
[7] Chen Z, Niu X, Liu J, et al. Seismic study on an innovative fully-bolted beam-column joint in prefabricated modular steel buildings[J]. Engineering Structures, 2021, 234: 111875. 10.1016/j.engstruct.2021.111875
[8] Li G C, Chen B W, Yang Z J, et al. Axial behavior of high-strength concrete-filledhigh-strength square steel tubular stub columns[J]. Adv Steel Constr, 2021, 17(2): 158-168. 10.18057/IJASC.2021.17.2.6
[9] Yao Y, Huang H, Zhang W, et al. Seismic performance of steel-PEC spliced frame beam[J]. Journal of Constructional Steel Research, 2022, 197: 107456. 10.1016/j.jcsr.2022.107456
[10] Chen Y, Li W, Fang C. Performance of partially encased composite beams under static and cyclic bending[J]. Structures, 2017, 9(FEB.): 29-40. 10.1016/j.istruc.2016.09.004
[11] Jiang Y, Hu X, Hong W, et al. Experimental study and theoretical analysis of partially encased continuous composite beams[J]. Journal of Constructional Steel Research, 2016, 117: 152-160. 10.1016/j.jcsr.2015.10.009
[12] Wang Z, Ye Y, Ma Y, et al. Experimental and finite element flexural performance study of HPEC beam[J]. Journal of Constructional Steel Research, 2023, 211: 108189. 10.1016/j.jcsr.2023.108189
[13] Ahn J K, Lee C H. Fire behavior and resistance of partially encased and slim-floor composite beams[J]. Journal of Constructional Steel Research, 2017, 129: 276-285. 10.1016/j.jcsr.2016.11.018
[14] He J, Wang S, Liu Y, et al. Mechanical behavior of a partially encased composite girder with corrugated steel web: Interaction of shear and bending[J]. Engineering, 2017, 3(6): 806-816. 10.1016/j.eng.2017.11.005
[15] Piloto P A G, Ramos-Gavilán A B, Gonçalves C, et al. Experimental bending tests of partially encased beams at elevated temperatures[J]. Fire Safety Journal, 2017, 92: 23-41. 10.1016/j.firesaf.2017.05.014

[16] Nakamura S, Momiyama Y, Hosaka T, et al. New technologies of steel/concrete composite bridges[J]. Journal of Constructional Steel Research, 2002, 58(1): 99-130. 10.1016/s0143-974x(01)00030-x
[17] He J, Liu Y, Lin Z, et al. Shear behavior of partially encased composite I-girder with corrugated steel web: Numerical study[J]. Journal of Constructional Steel Research, 2012, 79: 166-182. 10.1016/j.jcsr.2012.07.018
[18] He J, Liu Y, Chen A, et al. Bending behavior of concrete-encased composite I-girder with corrugated steel web[J]. Thin-walled structures, 2014, 74: 70-84. 10.1016/j.tws.2013.08.003
[19] De Nardin S, El Debs A L H C. Study of partially encased composite beams with innovative position of stud bolts[J]. Journal of Constructional Steel Research, 2009, 65(2): 342-350. 10.1016/j.jcsr.2008.03.021
[20] Kindmann R, Bergmann R, Cajot L G, et al. Effect of reinforced concrete between the flanges of the steel profile of partially encased composite beams[J]. Journal of Constructional Steel Research, 1993, 27(1-3): 107-122. 10.1016/0143-974x(93)90009-h
[21] Barros J A O, Figueiras J A. Flexural behavior of SFRC: testing and modeling[J]. Journal of materials in civil engineering, 1999, 11(4): 331-339. 10.1061/(ASCE)0899-1561(1999)11:4(331)
[22] Li V C. Engineered cementitious composites (ECC) material, structural, and durability performance[M]. 2008.
[23] Yoo D Y, Yoon Y S. Structural performance of ultra-high-performance concrete beams with different steel fibers[J]. Engineering Structures, 2015, 102: 409-423. 10.1016/j.engstruct.2015.08.029
[24] Hao N, Yang Y, Xue Y, et al. Shear performance of partially encased composite beams with high-strength steel and UHPC[J]. Journal of Constructional Steel Research, 2023, 211: 108217. 10.1016/j.jcsr.2023.108217
[25] Zhao B, Huo H, Ran C, et al. Flexural behavior of castellated partially encased composite (PEC) beams[J]. Journal of Constructional Steel Research, 2024, 214: 108509. 10.1016/j.jcsr.2024.108509
[26] Technical specification for partially clad steel-concrete composite structures: T/CECS 719-2020 [S]. Beijing: China Architecture and Construction Press, 2020. (in Chines)
[27] Test method standard for physical and mechanical properties of concrete: GB/T50081-2019[S]. Beijing: Standards Press of China, 2019. (in Chines)
[28] Tensile test method for metal materials at room temperature GB/T 228-2010 [S]. Beijing: Standards Press of China, 2010. (in Chines)
[29] Chang Xinquan, Wang Xin, Liu Changyuan, Wu Zhishen. Reliability evaluation of finite element Model for flexural performance of RC beams reinforced by Prestressed FRP plates [J]. Journal of Nanjing University of Technology (Natural Science Edition), 2021, 43(03): 318-328. (in Chines)
[30] Specification for design of concrete structures: GB 50010-2010 [S]2015 edition. Beijing: China Architecture and Construction Press, 2015. (in Chines)
[31] Rao G A, Vijayanand I, Eligehausen R. Studies on ductility of RC beams in flexure and size effect [C] // Proceedings of the 6th International Conference on Fracture Mechanics of Concrete and Concrete Structures. Catania: 2017.
[32] Zheng XF. Experimental Study on Dimensional effect of bending performance of high-strength concrete beams [D]. Dalian: Dalian University of Technology, 2011. (in Chines)
[33] Alca N, Alexander S D B, MacGregor J G. Effect of size on flexural behavior of high-strength concrete beams[J]. Structural Journal, 1997, 94(1): 59-67. 10.14359/461